THE JOURNAL OF PHYSICAL CHEMISTRY A

Article

Cite This: J. Phys. Chem. A 2019, 123, 4543−4554

pubs.acs.org/JPCA

Molecular Dynamics Simulations on Relaxed Reduced-Dimensional Potential Energy Surfaces

Chang Liu,[†] C. T. Kelley,*[,‡] and Elena Jakubikova*[,†]

[†]Department of Chemistry and [‡]Department of Mathematics, North Carolina State University, Raleigh, North Carolina 27695, United States

Supporting Information

ABSTRACT: Molecular dynamics (MD) simulations with full-dimensional potential energy surfaces (PESs) obtained from high-level ab initio calculations are frequently used to model reaction dynamics of small molecules (i.e., molecules with up to 10 atoms). Construction of full-dimensional PESs for larger molecules is, however, not feasible since the number of ab initio calculations required grows rapidly with the increase of dimension. Only a small number of coordinates are often essential for describing the reactivity of even very large systems, and reduced-dimensional PESs with these coordinates can be built for reaction dynamics studies. While analytical methods based on transition-state theory framework are well established for analyzing the reduced-dimensional PESs, MD simulation algorithms capable of generating trajectories on such surfaces are more rare. In this work, we present a new MD implementation that utilizes the relaxed reduced-dimensional PES for standard microcanonical (NVE) and canonical (NVT) MD simulations. The method is applied to the pyramidal inversion of a NH_3 molecule. The results from the MD simulations on a reduced, three-dimensional PES are validated against the ab initio MD simulations, as well as MD simulations on full-dimensional PES and experimental data.

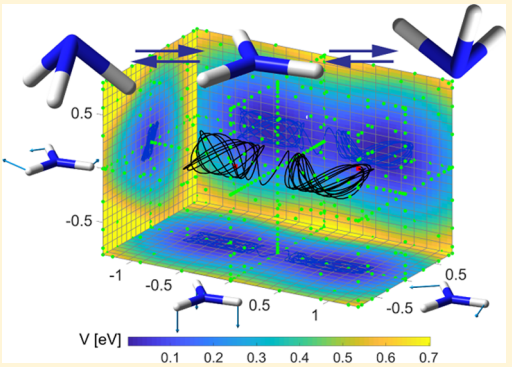

1. INTRODUCTION

Molecular dynamics (MD) simulations, first introduced by Alder and Wainwright in 1959,[1] have been utilized to study equilibrium and nonequilibrium phenomena for systems with various sizes, including but not limited to simple molecules in a uniform-phase environment or at the interface,[2−7] polymers,[8−11] biomolecules,[12−20] and solid-state materials.[21−28] Most MD methods are based on the Born−Oppenheimer (BO) approximation.[29,30] With the BO approximation, the nuclei of atoms in a molecule are moving in the average field of electrons, which is known as the potential energy surface (PES). As a result, MD implementations are typically composed of two building blocks: the approximation of the PES and the propagation of atomic positions. Depending on equations of motion used, the propagation algorithms can be roughly divided into three types: (1) classical algorithms that are ruled by Newton's laws,[1] (2) quantum algorithms that employ Schrödinger equation,[31−34] and (3) quasi-classical algorithms that apply additional zero-point vibrational corrections and tunneling effects to classical algorithms.[35−41] In this paper, we will focus on classical methods as only the classical or quasi-classical methods are feasible for large systems, and quasi-classical methods can be easily adapted from classical methods.[37]

Different methods have been developed to obtain the PES for MD simulations. The most straightforward way to compute PES is to carry out electronic structure calculations at each MD step. Methods based on this "on-the-fly" calculation strategy are called ab initio MD and are often applied to study reaction dynamics of small systems.[42,43] For larger systems, it is not feasible to apply ab initio MD simulations because high-level electronic structure calculations become too expensive. As a result, more efficient methods to obtain information about the PES are required. The force field methods, which represent the potential energy as a sum of different contributions with empirical function forms, are widely used on simulations of biomolecules and polymers.[8−13,15,16,18−20] However, improving the accuracy of force field parameters to match the experimental and ab initio MD results is, for some cases, hard to achieve because of the limitation of functional form that describes different types of interactions and the requirement for parameters to be transferrable among different systems.[44−46] To efficiently carry out reliable MD simulations in these situations, different approaches have been developed to approximate the PES of a specified system, including, but not limited to, the modified Shepard interpolation method developed by Collins,[47−49] permutationally invariant potential energy surface by linear least-square fitting developed by Braams and Bowman,[4,45,50−53] neural network approaches,[54−56] Gaussian process,[57,58] and finite element

Received: March 11, 2019
Revised: April 29, 2019
Published: April 30, 2019

DOI: 10.1021/acs.jpca.9b02298
J. Phys. Chem. A 2019, 123, 4543−4554

method.[59−61] The size of a system that can be treated by these full-dimensional PES (f-PES) MD methods is very limited because the computational cost increases rapidly with the increase of degrees of freedom (dofs).

On the other hand, often only a small number of dofs is important for describing a reaction in a large system. These significant dofs are called "reaction coordinates", while all other coordinates are assumed to have no net contribution to the reaction.[62] As a result, relaxed reduced-dimensional PESs (rr-PESs) with a limited number of reaction coordinates are widely used for studying the reactions within the transition-state theory framework.[63] Ideally, one would like to be able to employ such rr-PESs to study reaction dynamics and generate MD trajectories on these surfaces. However, because rr-PESs are built with only a small number of coordinates, they do not contain sufficient information to describe the conformation of the entire system and it is not straightforward to carry out the MD simulation on the rr-PES. Recently, we have developed a method to approximate the rr-PES of an arbitrary system using the sparse grid Smolyak interpolation algorithm.[64−66] In this work, we will present algorithms to generate classical trajectories on rr-PESs. The method separates the design variables utilized for building rr-PES and remainder variables. The equations of motion in Hamiltonian formalism for design variables are solved to generate classical trajectories in the NVE ensemble. Additionally, Andersen and Langevin thermostat algorithms are adapted for simulations of the NVT ensemble on rr-PES. The method is implemented in MATLAB. Pyramidal inversion of NH_3 molecule is used as a test case to validate the rr-PES MD algorithm.

2. DESCRIPTION OF THE MD ON THE RELAXED REDUCED-DIMENSIONAL PES

2.1. Construction of rr-PES with Smolyak Interpolation Algorithm. In this work, the Smolyak interpolation algorithm is utilized to construct rr-PES along with the interpolants for Cartesian and internal coordinates of the system. Here, we only outline the main features of the interpolation approach, but a detailed description of the Smolyak interpolation algorithm can be found in refs 67−69. Examples of how this algorithm can be applied to systems of chemical interest with more than 10 atoms are in refs 64−66.

Consider a system with N atoms. Its position in space is defined by a $3N$-dimensional vector of Cartesian coordinates $\mathbf{x} = (x_1, x_2, ..., x_{3N})$. The electronic energy, V_i, of this system at any electronic state $i = 0, 1, 2, ...$ can be computed as a function of $\mathbf{x}$. While in this work we focus only on the ground-state potential energy surface of the system (V_0, labeled as V from this point forward), the PES construction and MD implementation on the excited-state PESs can be done in a completely analogous manner.

To build the n-dimensional rr-PES, a set of n design variables are chosen based on the chemical knowledge of the system. These design variables are a subset of $3N - 6$ internal coordinates, defined in terms of the bond lengths, bond angles, torsional angles, or a subset of normal mode coordinates defined at a particular point of the PES. The configuration vector of the system, $\mathbf{r} = (\mathbf{q}, \boldsymbol{\xi})$, is partitioned into a vector of design variables (or reaction coordinates) $\mathbf{q} \in \mathbb{R}^n$ and a vector of the remainder variables $\boldsymbol{\xi} \in \mathbb{R}^{3N-6-n}$. The n-dimensional rr-PES is built via the constrained optimization

$$V(\mathbf{q}_i) = \min_{\boldsymbol{\xi}} E(\mathbf{q}_i, \boldsymbol{\xi}) \tag{1}$$

where the minimization is carried over the remainder variables $\boldsymbol{\xi}$ at a set of sparse grid points. Each point on a grid corresponds to a specific vector of design variables $\mathbf{q}_i$. The constrained optimizations also determine the value of the remainder variables $\boldsymbol{\xi}(\mathbf{q}_i)$ and Cartesian coordinates $\mathbf{x}(\mathbf{q}_i)$ at each grid point $\mathbf{q}_i$. While $\boldsymbol{\xi}(\mathbf{q}_i)$ is unique, $\mathbf{x}(\mathbf{q}_i)$ is not unique since the translation or rotation of the system in three-dimensional space will produce a system with identical electronic energy. To obtain a consistent set of Cartesian coordinates at each grid point, we choose a set of $\mathbf{x}(\mathbf{q}_i)$ that translates and rotates all structures in a manner that minimizes the root-mean-square deviation between the geometry obtained at each grid point $\mathbf{q}_i$ and an arbitrary reference geometry $\mathbf{x}_0$

$$\mathbf{x}(\mathbf{q}_i) = \underset{\mathbf{x}|\mathbf{r}(\mathbf{x})=(\mathbf{q}_i,\boldsymbol{\xi}(\mathbf{q}_i))}{\operatorname{argmin}} \sqrt{\frac{1}{3N}(\mathbf{x}-\mathbf{x}_0)^{\mathrm{T}}\mathbf{m}(\mathbf{x}-\mathbf{x}_0)} \tag{2}$$

In the above, $\mathbf{m}$ is a $3N$ by $3N$ diagonal matrix, with diagonal elements, $m_{k,k} = m_k$, that correspond to the mass associated with the atom described by a coordinate x_k. Note that any electronic structure method can be utilized to perform the constrained optimizations necessary to evaluate the energies and obtain optimized structures of the system at each point of the grid.

The sparse grid points utilized in Smolyak's interpolation algorithm are uniquely specified by n, a polynomial degree of exactness k, and a domain of interpolation d. The number of grid points grows only polynomially with the dimension instead of exponentially. The grids are also nested in k, which means that all of the evaluations of $V(\mathbf{q})$, $\boldsymbol{\xi}(\mathbf{q})$, or $\mathbf{x}(\mathbf{q})$ from the k sparse grid, which correspond to expensive electronic structure calculations, can be reused to obtain an approximation on the $k + 1$ sparse grid. Using the calculated energies or coordinates at each sparse grid point as an input, the interpolation algorithm constructs an interpolating polynomial from a linear combination of interpolating polynomials on different "levels" of grids. In this way, interpolating polynomials can be obtained for $V(\mathbf{q})$, creating an rr-PES, but also for each coordinate $\boldsymbol{\xi}_i(\mathbf{q})$ or $x_i(\mathbf{q})$, allowing one to interpolate the molecular structure in between the grid points, which is necessary for performing MD simulations. By utilizing the reformulation of Smolyak's algorithm[69] and recursive Lagrange basis polynomials, the interpolation algorithm employed in this work can evaluate the functional values and analytical gradients efficiently.[66] Compared to methods that are designed specifically for potential energy surface fitting, such as permutationally invariant polynomial-based methods,[45,51,53,54] the Smolyak interpolation algorithm provides a more flexible functional form, which is suitable for representing not only $V(\mathbf{q})$ but also $\boldsymbol{\xi}(\mathbf{q})$ and $\mathbf{x}(\mathbf{q})$. The cost of the Smolyak algorithm is too large for high-dimensional surfaces ($d > 10$ and $k > 5$).[66] While one may be tempted by other general fitting or interpolation algorithms, such as Gaussian process[57,58] or neural network models,[55,56] these approaches do not have the accuracy needed for this application. We know of no other method that will provide a high-dimensional surrogate model having the precision that this application requires.

2.2. General Approach to MD Simulations on rr-PES. Once the rr-PES is constructed, the classical equations of

DOI: 10.1021/acs.jpca.9b02298
J. Phys. Chem. A 2019, 123, 4543−4554

Scheme 1. Flowchart for NVE MD Simulations

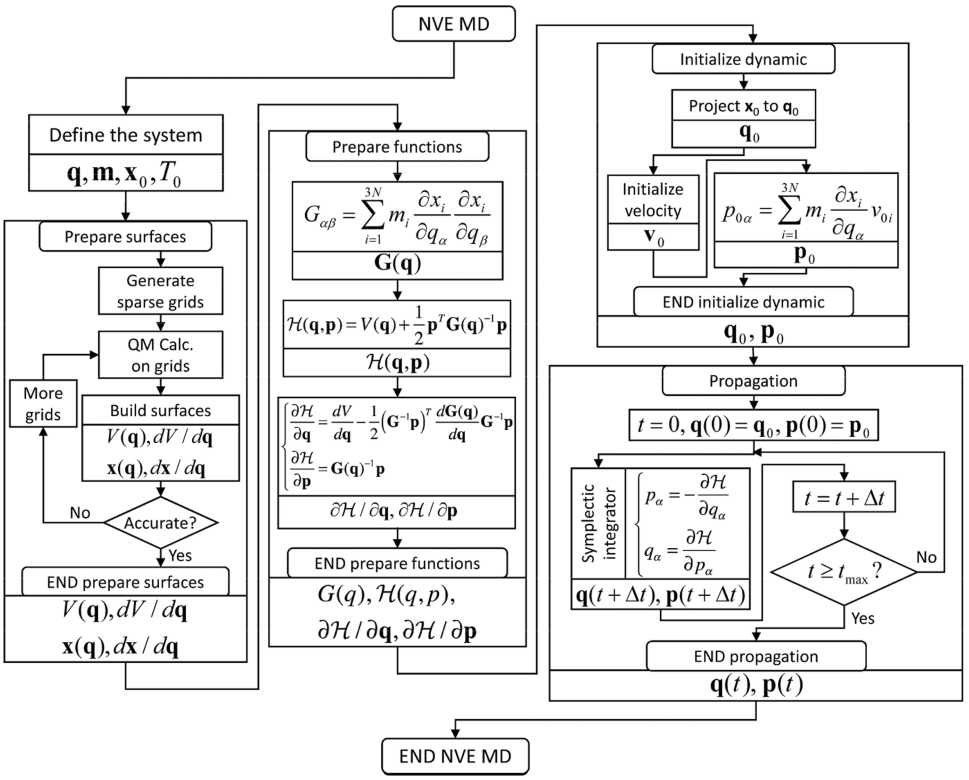

motion in Hamiltonian formalism[70,71] can be used to describe the trajectory along the n-dimensional reaction coordinate defined by a vector of design variables $\mathbf{q} = (q_1, q_2, ..., q_n)$ and its conjugate momentum vector $\mathbf{p} = (p_1, p_2, ..., p_n)$. The time evolution of the system on rr-PES is described by Hamilton's equations of motion

$$\dot{q}_\alpha = \frac{\partial \mathcal{H}}{\partial p_\alpha}, \quad \alpha = 1, 2, ..., n \tag{3}$$

$$\dot{p}_\alpha = -\frac{\partial \mathcal{H}}{\partial q_\alpha}, \quad \alpha = 1, 2, ..., n \tag{4}$$

where $\mathcal{H} = \mathcal{H}(\mathbf{q}, \mathbf{p})$ is the Hamiltonian, and the overdot denotes the time derivative. The Hamiltonian also represents the total energy of the system composed of the potential (V) and kinetic (K) energies

$$\mathcal{H}(\mathbf{q}, \mathbf{p}) = V(\mathbf{q}) + K(\mathbf{q}, \mathbf{p}) \tag{5}$$

The potential energy term, $V(\mathbf{q})$, can be directly obtained from the sparse grid rr-PES, while the kinetic energy is defined in terms of the momentum and the mass-metric tensor $\mathbf{G}(\mathbf{q})$

$$K(\mathbf{q}, \mathbf{p}) = \frac{1}{2}\mathbf{p}^T\mathbf{G}^{-1}\mathbf{p} \tag{6}$$

$$G_{ij} = \sum_{k=1}^{3N} m_k \frac{\partial x_k}{\partial q_i}\frac{\partial x_k}{\partial q_j} \tag{7}$$

In the above, m_k corresponds to the mass associated with the atom described by a coordinate x_k. Note that while $\mathbf{G}$ is a matrix with $n \times n$ dimensions, each element of $\mathbf{G}$ depends on the $3N$ Cartesian coordinates of the entire system. The Cartesian coordinate vector at each point of the rr-PES, $\mathbf{x}(\mathbf{q})$, is obtained from Smolyak's interpolation algorithm, as described above, and the derivatives needed to obtain G_{ij} are computed analytically from the interpolating function on the fly. Note that the interpolation of Cartesian coordinates with polynomial basis is inefficient and inaccurate for certain design variables, such as internal rotations. In those cases, other basis, such as trigonometric functions, can be employed for the interpolation algorithm.

2.3. NVE Simulations on the rr-PES. To perform the MD simulations in which the energy is conserved (i.e., in the NVE ensemble), the analytical form of the rr-PES, $V(\mathbf{q})$, is needed, along with a Cartesian coordinate vector $\mathbf{x}(\mathbf{q})$ at each point of the rr-PES. Having chosen the initial conditions for the simulation at time $t = 0$, $(\mathbf{q}_0, \mathbf{p}_0)$, we employ a symplectic Störmer–Verlet algorithm[72,73] to propagate the positions and momenta on the rr-PES

$$\mathbf{q}_{n+1/2} = \mathbf{q}_n + \frac{\Delta t}{2}\left.\frac{\partial \mathcal{H}(\mathbf{q}, \mathbf{p})}{\partial \mathbf{p}}\right|_{\mathbf{q}_{n+1/2}, \mathbf{p}_n} \tag{8}$$

$$\mathbf{p}_{n+1} = \mathbf{p}_n - \frac{\Delta t}{2}\left(\left.\frac{\partial \mathcal{H}(\mathbf{q}, \mathbf{p})}{\partial \mathbf{q}}\right|_{\mathbf{q}_{n+1/2}, \mathbf{p}_n} + \left.\frac{\partial \mathcal{H}(\mathbf{q}, \mathbf{p})}{\partial \mathbf{q}}\right|_{\mathbf{q}_{n+1/2}, \mathbf{p}_{n+1}}\right) \tag{9}$$

$$\mathbf{q}_{n+1} = \mathbf{q}_{n+1/2} + \frac{\Delta t}{2}\left.\frac{\partial \mathcal{H}(\mathbf{q}, \mathbf{p})}{\partial \mathbf{p}}\right|_{\mathbf{q}_{n+1/2}, \mathbf{p}_{n+1}} \tag{10}$$

The derivatives of Hamiltonian are obtained as

DOI: 10.1021/acs.jpca.9b02298
J. Phys. Chem. A 2019, 123, 4543−4554

$$\frac{\partial \mathcal{H}(\mathbf{q}, \mathbf{p})}{\partial \mathbf{q}} = \frac{\partial V(\mathbf{q})}{\partial \mathbf{q}} - \frac{1}{2}(\mathbf{G}^{-1}(\mathbf{q})\mathbf{p})^{\mathrm{T}} \frac{\partial \mathbf{G}(\mathbf{q})}{\partial \mathbf{q}} \mathbf{G}^{-1}(\mathbf{q})\mathbf{p} \tag{11}$$

$$\frac{\partial \mathcal{H}(\mathbf{q}, \mathbf{p})}{\partial \mathbf{p}} = \mathbf{G}^{-1}(\mathbf{q})\mathbf{p} \tag{12}$$

Since the Hamiltonian $\mathcal{H} = \mathcal{H}(\mathbf{q}, \mathbf{p})$ is nonseparable, the steps represented by eqs 8 and 9 have to be evaluated implicitly (with an iterative solver), which makes this approach less efficient. However, this method is accurate and straighforward to implement, and we have therefore chosen to employ it in this work. In the future, we plan to implement more efficient algorithms where all evaluations can be done explicitly, such as those based on generating functions.[74,75]

The full procedure and important equations for the NVE rr-PES MD are summarized in Scheme 1. The method is written in MATLAB, using the optimization toolbox to solve eqs 8 and 9.

2.4. Thermostat Algorithms in the rr-PES Approximation. For practical applications, it is desirable to perform MD simulations on rr-PES in a canonical (NVT) ensemble.[76] To properly model the canonical ensemble on rr-PES and achieve correct distribution of the thermodynamic properties, such as energy and temperature,[76] we adapt two commonly used thermostats, Andersen[77] and Langevin,[78] to MD simulations on rr-PES. Both of these thermostats can be easily implemented in a Cartesian coordinate system and are used with Cartesian coordinates in our case as well. Therefore, to apply the thermostat algorithms for simulations on rr-PES, we need to consider velocities in a Cartesian representation $\mathbf{v}_{\mathrm{all}}(\mathbf{q}, \mathbf{p}) = (v_1, ..., v_{3N})$. Each component of the velocity vector can be expressed as a sum of the velocity components due to the motion on rr-PES, $\mathbf{v}_{\mathrm{rr\text{-}PES}}$ and due to the motion of all of the other degrees of freedom, $\mathbf{v}_{\mathrm{other}}$

$$\mathbf{v}_{\mathrm{all}}(\mathbf{q}, \mathbf{p}) = \mathbf{v}_{\mathrm{rr\text{-}PES}}(\mathbf{q}, \mathbf{p}) + \mathbf{v}_{\mathrm{other}}(\mathbf{q}) \tag{13}$$

The Cartesian velocities due to the motion on rr-PES at a given point $[\mathbf{q}_i, \mathbf{p}_i]$ can be computed numerically according to

$$\mathbf{v}_{\mathrm{rr\text{-}PES}}(\mathbf{q}, \mathbf{p}) = \frac{\mathbf{x}(\mathbf{q} + h\dot{\mathbf{q}}(\mathbf{q}, \mathbf{p})) - \mathbf{x}(\mathbf{q} - h\dot{\mathbf{q}}(\mathbf{q}, \mathbf{p}))}{2h} \tag{14}$$

where h corresponds to the step size for numerical differentiation.

Because the velocities obtained from eq 14 are based on equations of motion on the rr-PES, the components of the velocity vector due to the motion along the other degrees of freedom ($\boldsymbol{\xi}$) are not accounted for. Therefore, we need to recover these velocity vector components before feeding them to the thermostat algorithms. This is done under the assumption that the motion along $\boldsymbol{\xi}$ has no memory and therefore its velocity components always follow the Maxwell–Boltzmann distribution. Therefore, we first use the Maxwell–Boltzmann distribution to assign velocities of all atoms at a particular temperature T, $\mathbf{v}^{\mathrm{M-B}}$

$$\mathbf{v}^{\mathrm{M-B}} = \sqrt{k_{\mathrm{B}} T \mathbf{m}^{-1}} \mathbf{R}_t \tag{15}$$

where $\mathbf{R}_t$ is a standard $3N$-dimensional Gaussian random variable generated at time t. The contributions that arise from the motion on rr-PES are then removed from $\mathbf{v}^{\mathrm{M-B}}$ to obtain the velocities of the other degrees of freedom at T due to the Maxwell–Boltzmann distribution

$$\mathbf{v}^{\mathrm{M-B}}_{\mathrm{other}}(\mathbf{q}) = \mathbf{v}^{\mathrm{M-B}} - \mathbf{v}_{\mathrm{rr\text{-}PES}}\left(\mathbf{q}, \frac{\mathrm{d}\mathbf{x}}{\mathrm{d}\mathbf{q}} \mathbf{m}\mathbf{v}^{\mathrm{M-B}}\right) \tag{16}$$

The recovered velocity, $\mathbf{v}^{\mathrm{M-B}}_{\mathrm{all}}$, at a given point is then obtained as

$$\mathbf{v}^{\mathrm{M-B}}_{\mathrm{all}}(\mathbf{q}, \mathbf{p}) = \mathbf{v}_{\mathrm{rr\text{-}PES}}(\mathbf{q}, \mathbf{p}) + \mathbf{v}^{\mathrm{M-B}}_{\mathrm{other}}(\mathbf{q}) \tag{17}$$

Velocities in this form are then employed in standard thermostat algorithms as described below.

2.4.1. Andersen Thermostat. The Andersen thermostat represents one of the simplest algorithms that can produce the correct energy and temperature distribution.[76] It assumes that the system is undergoing stochastic collisions, which reassign the atom velocities based on the Maxwell–Boltzmann distribution at a given temperature. The time intervals between successive collisions on one atom follow a distribution, $P(t)$, given by

$$P(t) = \nu \exp(-\nu t) \tag{18}$$

where ν determines the frequency of collisions and t is the time.

Our NVT simulations with the Andersen thermostat use the same algorithm to propagate momenta and positions along the rr-PES as the NVE simulations (see eqs 8–10). After each step of the NVE propagation, an N-dimensional vector of uniform random numbers is generated, $\eta = (\eta_1, ..., \eta_N)$, where $\eta_i \in [0, 1]$. The components of the velocity vector, $\mathbf{v}^{\mathrm{M-B}}_{\mathrm{all}}$ (obtained from eq 17), are then reassigned based on the Maxwell–Boltzmann distribution for each atom with $\eta_i < \nu\Delta t$ (where ν represents frequency from eq 26, and Δt is the time step), obtaining a new velocity vector $\mathbf{v}^{\mathrm{Andersen}}_{\mathrm{all}}$. The new momentum vector, $\mathbf{p}$, is generated based on these velocities as

$$\mathbf{p} = \frac{\partial \mathbf{x}}{\partial \mathbf{q}} \mathbf{m}\mathbf{v}^{\mathrm{Andersen}}_{\mathrm{all}} \tag{19}$$

The velocity recovery step that generates $\mathbf{v}^{\mathrm{M-B}}_{\mathrm{all}}$ (see eqs 16 and 17) is necessary for obtaining the correct energy distribution. The velocity reassignment will cause a kinetic energy exchange between $\mathbf{q}$ and $\boldsymbol{\xi}$. When the system is in equilibrium, the average net energy exchange between $\mathbf{q}$ and $\boldsymbol{\xi}$ must be zero. If the velocity recovery step is not included, the kinetic energy for $\boldsymbol{\xi}$ is equal to zero before the velocity reassignment and becomes positive after the velocity reassignment, indicating a nonzero net energy exchange between $\mathbf{q}$ and $\boldsymbol{\xi}$.

2.4.2. Langevin Thermostat. The Langevin thermostat is another widely used algorithm for NVT MD simulations. The equations of motion employed for MD simulations are the Langevin equations, which have two additional terms that mimic the coupling between the system and a thermal bath.[79] The Langevin equations in Cartesian coordinates can be written as

$$\mathrm{d}\mathbf{q}_i = \frac{\partial \mathcal{H}}{\partial \mathbf{p}_i} \mathrm{d}t$$

$$\mathrm{d}\mathbf{p}_i = \mathbf{F}_i \mathrm{d}t - \gamma_i \mathbf{p}_i \mathrm{d}t + \sigma_i \mathrm{d}\mathbf{w} \tag{20}$$

where $\mathbf{q}_i$ and $\mathbf{p}_i$ represent the position and momentum of the atom i, respectively, and $\mathbf{F}_i = -\partial \mathcal{H}/\partial \mathbf{q}_i$ is the force on the atom i. The last two terms represent the frictional forces

DOI: 10.1021/acs.jpca.9b02298
J. Phys. Chem. A 2019, 123, 4543–4554

($-\gamma_i \mathbf{p}_i$) and random forces ($\sigma_i \, d\mathbf{w}$), and without these, eq 20 would be identical to Newton's equations of motion. The symbol $\mathbf{w}$ represents a $3N$-dimensional Wiener process. The damping constant, γ_i, is related to the diffusion coefficient D_i according to the following formula

$$\gamma_i = \frac{k_B T}{m_i D_i} \tag{21}$$

To mimic the effect of the surrounding environment, we need to specify a unique γ_i value for each atom. However, as we only control the temperature, a common value γ is set for all atoms.[76]

The coefficient σ_i found in the random force term is determined from the fluctuation−dissipation theorem[79,80]

$$\sigma_i = \sqrt{2\gamma m_i k_B T} \tag{22}$$

We employ BAOAB procedure of Leimkuhler and Matthews[80,81] to solve eq 20, which splits Störmer−Verlet algorithm (see eqs 8−10) into two symplectic Euler integrators (BA, AB) and inserts the exact solution for the force-free Langevin equation for momentum (O) in between the two. These equations are then adapted to the rr-PES MD

$$\left.\begin{aligned} \mathbf{p}_{n+1/2} &= \mathbf{p}_n - \frac{\Delta t}{2}\frac{\partial \mathcal{H}}{\partial \mathbf{q}}\bigg|_{\mathbf{q}_n, \mathbf{p}_{n+1/2}} \\ \mathbf{q}_{n+1/2} &= \mathbf{q}_n + \frac{\Delta t}{2}\frac{\partial \mathcal{H}}{\partial \mathbf{p}}\bigg|_{\mathbf{q}_n, \mathbf{p}_{n+1/2}} \end{aligned}\right\} \text{Euler(BA)} \tag{23}$$

$$\left.\begin{aligned} \mathbf{p}_{\text{Cart}} &= e^{-\gamma \Delta t}\mathbf{m}\mathbf{v}_{\text{all}}^{\text{M-B}} + \sqrt{1 - e^{-2\gamma \Delta t}} \cdot \sqrt{\mathbf{m} k_B T}\,\mathbf{R}_t \\ \mathbf{p}'_{n+1/2} &= \left(\frac{\partial \mathbf{x}}{\partial \mathbf{q}}\right)^{\mathrm{T}}_{\mathbf{q}_{n+1/2}} \mathbf{p}'_{\text{Cart},n+1/2} \end{aligned}\right\} \text{O} \tag{24}$$

$$\left.\begin{aligned} \mathbf{q}_{n+1} &= \mathbf{q}_{n+1/2} + \frac{\Delta t}{2}\frac{\partial \mathcal{H}}{\partial \mathbf{p}}\bigg|_{\mathbf{q}_{n+1}, \mathbf{p}'_{n+1/2}} \\ \mathbf{p}_{n+1} &= \mathbf{p}'_{n+1/2} - \frac{\Delta t}{2}\frac{\partial \mathcal{H}}{\partial \mathbf{q}}\bigg|_{\mathbf{q}_{n+1}, \mathbf{p}'_{n+1/2}} \end{aligned}\right\} \text{Euler(AB)} \tag{25}$$

In the above, eqs 23 and 25 are the same as in the traditional BAOAB method, but in our case, reaction coordinates $\mathbf{q}$ rather than Cartesian coordinates are used for the propagation. The velocities employed in eq 24 now correspond to the "recovered" velocities (also see eq 17) obtained at the half-step

$$\mathbf{v}_{\text{all}}^{\text{M-B}} = \mathbf{v}_{\text{rr-PES}}(\mathbf{q}_{n+1/2}, \mathbf{p}_{n+1/2}) + \mathbf{v}_{\text{other}}^{\text{M-B}}(\mathbf{q}_{n+1/2}) \tag{26}$$

The velocity recovery step is redundant for the Langevin thermostat algorithm with a common value of the damping constant γ. This step is kept in eq 24 to make the form of the Langevin algorithm consistent with the case when different damping constants are used for different atoms. With a common γ, the "O" part of the Langevin algorithm can be more efficiently implemented as

$$\mathbf{p}'_{n+1/2} = e^{-\gamma \Delta t}\mathbf{p}_{n+1/2} + \sqrt{1 - e^{-2\gamma \Delta t}}\left(\frac{\partial \mathbf{x}}{\partial \mathbf{q}}\right)^{\mathrm{T}}_{\mathbf{q}_{n+1/2}} \sqrt{\mathbf{m} k_B T}\,\mathbf{R}_t \tag{27}$$

3. RESULTS: PYRAMIDAL INVERSION OF AMMONIA

The pyramidal inversion of ammonia (see Figure 1) is a suitable example to test our simulation algorithms for two

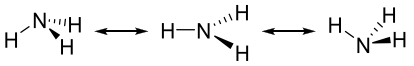

Figure 1. Pyramidal inversion of NH_3.

reasons. First, the ammonia molecule only has six internal degrees of freedom, which is small enough to build an f-PES or carry out ab initio MD simulations. Therefore, we can validate the results of rr-PES MD simulations against the more accurate ab initio MD or MD simulations on f-PES. Second, because the pyramidal inversion of an ammonia molecule does not involve significant N−H bond length changes, it is natural to build an rr-PES with the remaining degrees of freedom that include the umbrella inversion mode and two H−N−H scissoring modes.

3.1. Construction of f-PES and rr-PES. Geometry optimizations were carried out to obtain the ground- and transition-state structures of a singlet NH_3 molecule. All of these and the following electronic structure calculations were performed with the Gaussian 09 software package[82] utilizing the B3LYP functional[83−86] and 6-311g** basis sets[87−89] in vacuum. Follow-up frequency analyses were applied to both optimized geometries. All six normal modes of the ground-state structure (trigonal pyramidal) have real frequencies, indicating that a proper minimum energy conformation was achieved. For the transition-state structure (planar triangular), one out of six frequencies of normal modes is imaginary.

Normal modes (λ_i) of the trigonal planar structure (the transition state) are shown in Figure 2. The imaginary mode

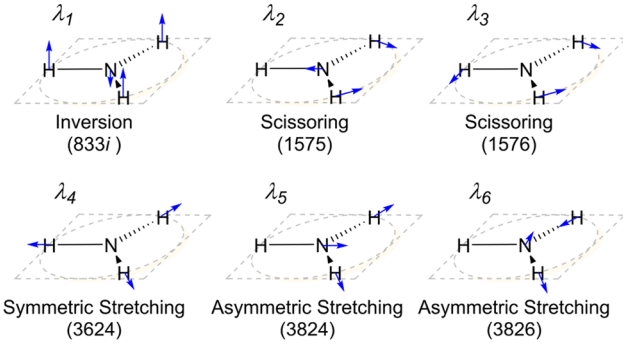

Figure 2. Normal modes of planar NH_3. The blue arrows represent atom displacements along each normal mode. Frequencies for each mode are listed in parentheses with unit cm^{-1}.

(λ_1) corresponds to the pyramidal inversion mode that connects the two stable trigonal pyramidal conformations. As a result, the selected coordinates for PESs need to describe this mode accurately at the trigonal planar conformation. To satisfy this constraint, we utilize all six normal coordinates (λ_1−λ_6) to

DOI: 10.1021/acs.jpca.9b02298
J. Phys. Chem. A 2019, 123, 4543−4554

build the f-PES and adapt the first three normal coordinates (λ_1–λ_3) to build the rr-PES.

In the full-dimensional case (n = 6), the geometry of a grid point on PES, $\mathbf{r}_i$, is represented as a sum of displacements along each normal coordinate, λ_i, from the trigonal planar structure, $\mathbf{x}_0$

$$\mathbf{r}_i = \mathbf{x}_0 + \sum_{i=1}^{6} q_i \lambda_i \tag{28}$$

A single-point energy calculation at the B3LYP/6-311G** level was performed at each grid point. The resulting geometries and energies were then utilized to build the f-PES with the method described in the Description of the MD on the Relaxed Reduced-Dimensional PES section. The interpolation domains for the six normal mode coordinates were chosen to be $q_1 \in [-1.30, 1.30]$, $q_2 \in [-0.80, 0.80]$, $q_3 \in [-0.80, 0.80]$, $q_4 \in [-0.17, 0.50]$, $q_5 \in [-0.17, 0.17]$, and $q_6 \in [-0.17, 0.17]$, where q_i represents displacements along the normal mode coordinate vectors.

In the reduced-dimensional case, modes λ_2 and λ_3 were utilized to build the rr-PES in addition to λ_1, since they all share the H–N–H angle changes and play an important role in the energy relaxation of the inversion motion when $|q_1| > 0.6$ (see Figure S1, Supporting information). The geometry at each grid point was prepared as follows. First, we built unrelaxed conformations by displacing the planar NH_3 structure along the three normal mode coordinates as in the f-PES construction. Then, the relaxed geometries were generated via the constrained optimization. In the constrained optimization step, the three N–H bond lengths [r(N–H)] were relaxed, while two H–N–H angles (θ) and bending angles (ω) (see Figure 3) were restricted to the unrelaxed values. The interpolation domains for λ_1–λ_3 modes were identical to those in the f-PES case.

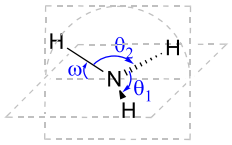

Figure 3. Internal coordinates constrained during the rr-PES optimization.

Both f-PES and rr-PES were built with k = 5 exactness employing the Smolyak algorithm introduced in the previous section. The grid points for f-PES and rr-PES can be found in the Supporting Information, see p S6. Table 1 compares the energy barrier ($E_{barrier}$), ω, average N–H distance ($\langle r$(N–H)$\rangle$), and average of two H–N–H angles ($\langle\theta\rangle$, see Figure 3) of the ground- and transition-state structures from f-PES, rr-PES, and density functional theory (DFT) calculations. In the following, the average value of a property f will be denoted as $\langle f\rangle$. All parameters from both f-PES and rr-PES agree with the DFT values, indicating that the two PESs with k = 5 exactness are sufficiently accurate.

Table 1. $E_{barrier}$ and $\langle r$(N–H)$\rangle$, $\langle\theta\rangle$, and ω for Ground State (gs) and Transition State (ts) from DFT, f-PES, and rr-PES[a]

	DFT	f-PES	rr-PES
$E_{barrier}$ (kcal/mol)	5.3543	5.3540	5.3545
$\langle r_{gs}$(N–H)$\rangle$ (Å)	1.0157	1.0154	1.0158
$\langle r_{ts}$(N–H)$\rangle$ (Å)	0.9987	0.9987	0.9987
$\langle\theta_{gs}\rangle$ (deg)	106.49	106.50	106.45
$\langle\theta_{ts}\rangle$ (deg)	120.00	120.00	120.00
ω_{gs} (deg)	61.66	61.45	61.73
ω_{ts} (deg)	0.00	0.00	0.00

[a]Results for different states are distinguished by subscripts.

3.2. NVE Simulations in rr-PES Approximation. To validate the NVE rr-PES MD algorithm, we compare the results obtained from the rr-PES MD with the results from f-PES MD and ab initio BOMD. Five trajectories were generated with each method using five different initial conditions. An initial geometry close to one of the global minima of the f-PES given by the vector of displacements along the normal mode coordinates

$$\mathbf{q}_0^f = [-0.5639,\ 0.0126,\ 0.0000,\ -0.1022,\ 0.0000,\ -0.0048]^T$$

was used as a starting structure for all five MD trajectories. The initial structure defined on f-PES was then converted to the Cartesian coordinates and projected onto the rr-PES to serve as the initial structure for BOMD and rr-PES MD. Five initial momenta in Cartesian coordinates were randomly generated for BOMD simulations using the Maxwell–Boltzmann distribution at 300 K. These Cartesian momenta were then projected and used as initial momenta for MD simulations on f-PES and rr-PES. Starting from these initial conditions, trajectories of 2.5 ps length were generated with the three different methods (BOMD, f-PES MD, and rr-PES MD) using a 0.025 fs time step.

3.2.1. Structural Parameters and Potential Energy Distribution. Figure 4 and Table 2 compare the distributions of potential energy ($V(\mathbf{q})$), ω, all three r(N–H), and θ obtained from all five trajectories for the three different methods. All four distributions from f-PES MD trajectories agree with the BOMD results. The agreement between the f-PES MD and BOMD distributions indicates that the

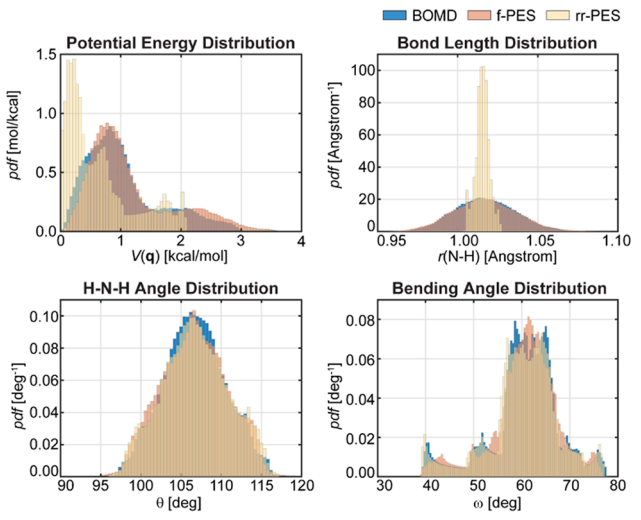

Figure 4. Potential energies, N–H bond lengths, H–N–H bond angles, and bending angle distributions. The area covered of each histogram is normalized to unity. The minimum value of potential energy on each surface was set to be zero.

DOI: 10.1021/acs.jpca.9b02298
J. Phys. Chem. A 2019, 123, 4543–4554

Table 2. Statistical Properties of Potential Energies, $V(\mathbf{q})$, N−H Bond Lengths, r(N−H), H−N−H Bond Angles, θ, and Bending Angles, ω

		BOMD	f-PES	rr-PES
$V(\mathbf{q})$ (kcal/mol)	range	[0.007, 3.054]	[0.004, 3.752]	[0.000, 2.070]
	mean	1.040	1.159	0.635
	stdev	0.637	0.712	0.557
r(N−H) (Å)	range	[0.961, 1.079]	[0.958, 1.094]	[1.005, 1.027]
	mean	1.017	1.017	1.015
	stdev	0.019	0.020	0.004
θ (deg)	range	[96.8, 116.6]	[94.3, 119.4]	[96.2, 117.1]
	mean	106.7	106.6	106.8
	stdev	3.9	4.1	4.1
ω (deg)	range	[39.3, 77.7]	[39.0, 76.9]	[39.2, 77.1]
	mean	60.6	60.6	60.3
	stdev	7.2	6.9	7.4

combination of f-PES with the Störmer−Verlet propagator generates accurate MD trajectories that are comparable to BOMD results in our implementation.

For rr-PES MD, only θ and ω have the distributions similar to the two full-dimensional methods (f-PES and BOMD). To justify the distribution of r(N−H), we exanimated the correlation between $\langle r(\text{N−H})\rangle$ and angle parameters, $[\langle\theta\rangle, \omega]$. As shown in Figure 5, although the rr-PES MD does not

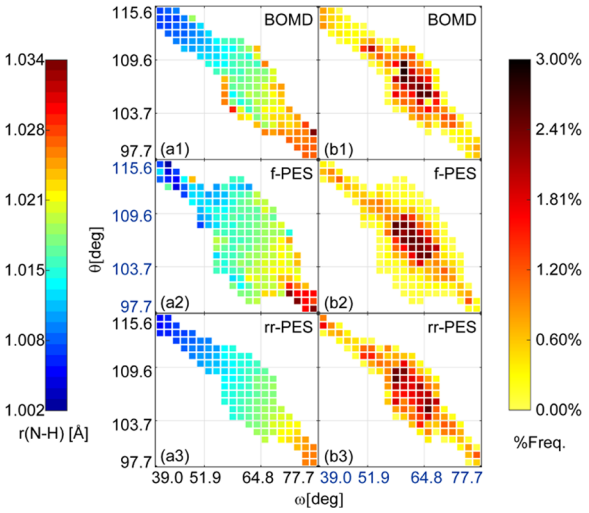

Figure 5. Correlation plots for geometry parameters. Plots (a1)−(a3) represent the average bond length in a given range of average theta and omega for BOMD, f-PES, and rr-PES, respectively. The distributions with a combination of θ and ω for different methods are shown in (b1)−(b3).

reproduce the distribution of r(N−H) from BOMD and f-PES MD, the rr-PES MD and full-dimensional MD methods produce similar average r(N−H) for a given combination of $\langle\theta\rangle$ and ω. Figure 5 also confirms that rr-PES MD produces the same distribution of $[\langle\theta\rangle, \omega]$ pair as the two full-dimensional MD methods. Note that the distributions from f-PES MD are broader than those obtained from BOMD and rr-PES MD results (see Figure 5). This is caused by the slight differences in both the PESs and initial conditions among different methods. Because the percentage of structures that are found in the edge regions of the f-PES plot is small, see Figure 5b1−b3, f-PES MD results are consistent with the BOMD and rr-PES results.

Due to the absence of the contributions from the degrees of freedom excluded from building the rr-PES ($\boldsymbol{\xi}$), rr-PES MD simulations result in a lower average value and standard deviation for potential energy distribution than full-dimensional MD results (see Figure 4 and Table 2). Noting that for any points on the rr-PES, forces along $\boldsymbol{\xi}$ are zero, there is no energy exchange between $\mathbf{q}$ (i.e., degrees of freedom used in building the rr-PES) and $\boldsymbol{\xi}$ along the trajectories on rr-PES. Assuming that the independence of $\mathbf{q}$ and $\boldsymbol{\xi}$ will hold for NVE ensembles, two subsystems described by $\mathbf{q}$ and $\boldsymbol{\xi}$ can be then described as two separate NVE ensembles. With this assumption, we are able to recover the full-dimensional potential energy distribution for an NVE rr-PES MD trajectory by adding in the contributions from $\boldsymbol{\xi}$, which can be randomly generated from the potential energy distribution of the $\boldsymbol{\xi}$ NVE ensemble, to potential energies at each step in the rr-PES trajectory. Figure 6 shows the recovered potential energy

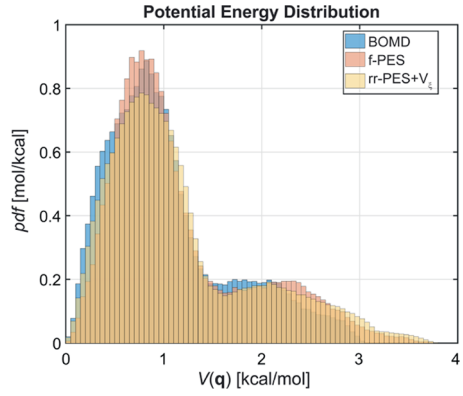

Figure 6. Potential energy distribution for rr-PES MD with bath potential fluctuation corrections.

distribution from rr-PES trajectories discussed above. The potential energy distribution of $\boldsymbol{\xi}$ is approximated as a uniform distribution in $[0, \mathcal{H}_{\boldsymbol{\xi}}]$, where the total energy of $\boldsymbol{\xi}$'s NVE ensemble for each trajectory was computed as the energy difference between f-PES and rr-PES, $\mathcal{H}_{\boldsymbol{\xi}} = \mathcal{H}_{\text{f-PES}} - \mathcal{H}_{\text{rr-PES}}$. The agreement between the recovered potential energy distribution of the rr-PES MD and distributions of full-dimensional methods verifies that $\mathbf{q}$'s contribution to the potential energy distribution is correctly reproduced by the rr-PES MD.

DOI: 10.1021/acs.jpca.9b02298
J. Phys. Chem. A 2019, 123, 4543−4554

3.2.2. Time-Dependent Properties. The results and discussion above demonstrated the capability of rr-PES MD to generate correct distributions of potential energy and geometric parameters that represent the full-dimensional system. Another important aspect of an MD method is the reproduction of time-dependent properties, which is mainly described by time-correlation functions.[90] Since, from the first-order perturbation theory, the line-shape function of IR is defined as the Fourier transform of the time-correlation function of dipole moment of the molecule,[90] we validated the time-dependent properties of our PES MD method by comparing the IR spectra obtained from the MD simulations with the experimental results.[91] Figure 7 shows the IR spectra

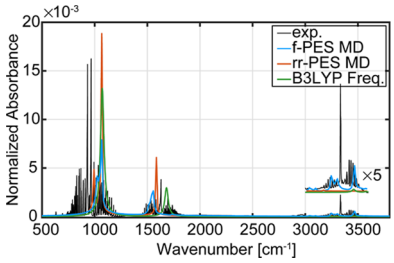

Figure 7. Experimental and computed IR spectra. Area covered by each spectrum was normalized to 1. Experimental IR spectrum is reproduced from reference 91, with the baseline set to zero. Each spectrum for PES MD is an average of results obtained from five trajectories. The IR spectrum from DFT frequency analysis is plotted with HWHM = 20 cm^{-1}. Absorption bands between 3000 and 3600 cm^{-1} were amplified by five times and are shown as an inset. Note that the B3LYP frequency analysis predicts a very weak absorption band at 3460 cm^{-1}, which can be barely seen from the plot.

predicted by f-PES and rr-PES MD trajectories. The dipole moments are computed from the interpolated partial charges from PESs. Computational details for simulated IR spectrum are summarized in Section S2, Supporting Information.

Experimental gas-phase IR spectrum displays three IR absorption bands. Both f-PES MD and rr-PES MD generate the two lower-energy bands, which correspond to the inversion and scissoring modes. The N−H stretching band, on the other hand, is only predicted by f-PES MD. This band is expected to be missing from the rr-PES MD simulations because the rr-PES MD suppresses the fluctuation of N−H bond lengths. The agreement between the PES-MD-predicted IR spectra and the experimental IR spectrum[91] as well as the DFT frequency analysis helps to validate the PES MD trajectories.

3.5. NVT Simulations in rr-PES Approximation. NVT rr-PES MD simulations with different target temperatures (100, 200, 300, 500, 750, 1000, 1500, and 2000 K) were carried out with the adapted Andersen and Langevin thermostats. Each simulation, except those for predicting the IR spectra, used a 1 fs step to generate a 40 ps trajectory. Simulations of 100 ps with a 1 fs step size were used to obtain the IR spectra for better resolution. To produce trajectories with realistic dynamical properties, both the collision frequency for Andersen thermostat and dumping constant for Langevin thermostat were set at a relatively small value, 0.001 fs^{-1}. The initial coordinates for each simulation were $\mathbf{q} = [0.589, 0.000, 0.000]$, at a structure that corresponds to a global minimum on the rr-PES. Initial momenta for each simulation were randomly selected from Maxwell−Boltzmann distribution of the target temperatures.

According to the equipartition theorem,[92] the average value and standard deviation of instantaneous temperature, $\mathcal{T} = 2K(\mathbf{q}, \mathbf{p})/nk_B$, are expected to be linear functions of the target temperature, T

$$\langle \mathcal{T} \rangle = T \tag{29}$$

$$\sqrt{\langle (\delta \mathcal{T})^2 \rangle} = \sqrt{2n^{-1}}\, T \approx 0.816T \tag{30}$$

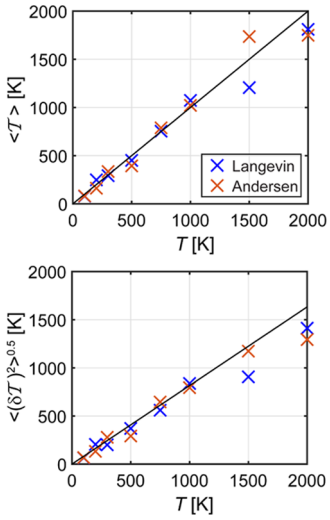

Figure 8. Average value and standard deviation of instantaneous temperature. The results for Langevin and Anderson were labeled with blue and red, respectively. The gray line represents the theoretically expected behavior.

Figure 8 shows the correlation plots for the average instantaneous temperature, $\langle \mathcal{T} \rangle$, and the standard deviation of instantaneous temperature, $\sqrt{\langle (\delta \mathcal{T})^2 \rangle}$, against the target temperature for NVT simulations with both Langevin and Andersen thermostats. The average value and standard deviation of $\mathcal{T}$ from both of these agree well with the theoretical expectations. These results confirm that the adapted thermostat algorithms are able to control the temperature correctly.

Another important property to validate is the accessible region in the configuration space with different target temperatures. Figure 9 shows the distributions of q_1 for given target temperatures on top of the projection of the rr-PES on q_1 direction with $q_2 = q_3 = 0$. The distribution of q_1 from rr-PES MD trajectories behaves just as expected: At low temperatures, only one of the potential energy wells is explored. With the increasing temperature, the covered region becomes larger. Finally, when the total energy is comparable to the energy barrier, the entire domain becomes accessible.

So far, we have shown that the NVT rr-PES MD with Langevin and Andersen thermostats are able to produce the correct canonical distributions. As in the case of NVE simulations, the validation of time-dependent properties will be done by comparing the predicted IR spectra from NVT rr-PES MD trajectories with the xsec-BYTe method[93−95] at different temperatures. Figure 10 shows the IR spectra from the rr-PES MD and xsec-BYTe.

DOI: 10.1021/acs.jpca.9b02298
J. Phys. Chem. A 2019, 123, 4543−4554

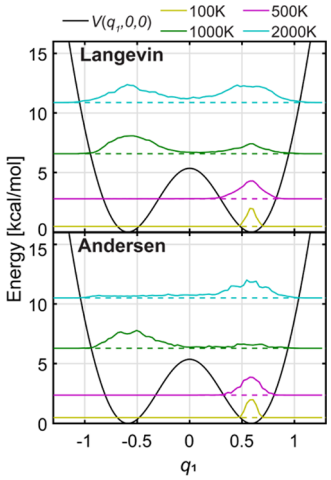

Figure 9. Projection of the rr-PES on q_1 direction (black lines), along with the distribution of q_1 from NVT rr-PES MD simulations at different temperatures (color lines) with Langevin and Andersen thermostats. The dashed lines represent the average total energies for each simulation, while the solid lines with different colors depict the probability density functions of q_1 for a given temperature.

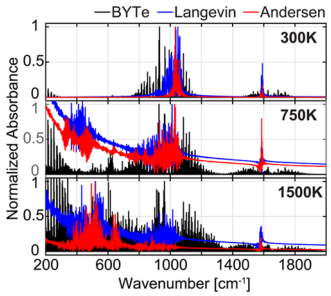

Figure 10. IR spectra obtained from the rr-PES MD simulations at different temperatures. The maximum peak between 500 and 1500 nm is normalized to 1.

At all target temperatures, IR spectra obtained from the MD simulations with Langevin and Andersen thermostats have similar shapes to BYTe spectra. At 300 K, both the positions and intensities of predicted spectra from the rr-PES MD agree with the BYTe results. At higher temperatures, rr-PES MD trajectories predict a strong absorption band at around 1 cm^{-1} (see Section S3, Supporting Information), which is assigned to the pyramidal inversion mode of ammonia.[96] As a result, the baselines of the IR spectra from rr-PES MD trajectories at higher temperatures are sloping down, making them different from the BYTe spectra. Besides this difference in baselines, spectra from rr-PES MD have the same trends as the BYTe spectra: more absorption bands appear in the region below 1000 cm^{-1} at higher temperatures, and their intensities increase with the increase in the temperature.

4. CONCLUSIONS

In this work, we have presented algorithms for NVE and NVT MD simulations on a relaxed reduced-dimensional potential energy surface, rr-PES, built by the Smolyak sparse interpolation algorithm.[67−69] The method utilizes the Hamiltonian formulation of classical mechanics to generate microcanonical trajectories on rr-PES. Two stochastic thermostat algorithms, Andersen and Langevin, were adapted to carry out MD simulations on rr-PES in the NVT ensemble.

Algorithms developed here were tested for NVE and NVT MD simulations on the ground-state potential energy surface of the ammonia molecule. The Smolyak sparse interpolation algorithm was utilized to construct both full-dimensional (6-D) and reduced-dimensional (3-D) PESs for NH_3. We have shown that our implementation of the MD algorithms on interpolated surfaces reproduces the correct distribution of structural properties, potential energy distribution, as well as time-dependent properties, such as IR spectra, obtained from ab initio Born−Oppenheimer MD simulations and experimental results.

Since the construction of rr-PESs requires significantly smaller number of accurate electronic structure calculations than the construction of f-PESs, the rr-PES MD algorithm is capable of generating classical trajectories for systems that are too large for full-dimensional simulations. Moreover, as the rr-PESs can be constructed for different electronic states of the system,[64,65] this approach can be further expanded to enable nonadiabatic MD simulations, for example, by utilizing a surface-hopping strategy, and MD-coupled quantum dynamics simulations.[97,98]

■ ASSOCIATED CONTENT

Supporting Information

The Supporting Information is available free of charge on the ACS Publications website at DOI: 10.1021/acs.jpca.9b02298.

Computational details of IR spectra calculations, lineshape functions for the pyramidal inversion band from NVT rr-PES MD simulations, and relaxed one-dimensional PES for the NH_3 inversion (PDF)

Data for f-PES and rr-PES grid points (XLSX)

■ AUTHOR INFORMATION

Corresponding Authors

*E-mail: ctk@ncsu.edu. Phone: 919-515-7163 (C.T.K.).
*E-mail: ejakubi@ncsu.edu. Phone: 919-515-1808 (E.J.).

ORCID

Chang Liu: 0000-0001-6008-7513
C. T. Kelley: 0000-0003-2791-0648
Elena Jakubikova: 0000-0001-7124-8300

Notes

The authors declare no competing financial interest.

■ ACKNOWLEDGMENTS

The authors gratefully acknowledge support from the National Science Foundation under Grant Nos. CHE-1554855 (C.L. and E.J.), DMS-1745654 and OAC-1740309 (C.T.K.). This work used the Extreme Science and Engineering Discovery Environment (XSEDE) Bridges at the Pittsburgh Supercomputing Center through Allocation No. TG-CHE170031 and the High-Performance Computing Center at NCSU. XSEDE is supported by the NSF ACI-1548562.[99]

■ REFERENCES

(1) Alder, B. J.; Wainwright, T. E. Studies in Molecular Dynamics. I. General Method. *J. Chem. Phys.* **1959**, *31*, 459−466.
(2) Garashchuk, S.; Rassolov, V. A.; Braams, B. J. Analytical Potential Energy Surface for $O+C_2H_2$ system. *Chem. Phys. Lett.* **2013**, *588*, 22−26.
(3) Monge-Palacios, M.; Rangel, C.; Espinosa-Garcia, J. *Ab Initio* Based Potential Energy Surface and Kinetics Study of the OH + NH_3

DOI: 10.1021/acs.jpca.9b02298
J. Phys. Chem. A 2019, 123, 4543−4554

Hydrogen Abstraction Reaction. *J. Chem. Phys.* **2013**, *138*, No. 084305.
(4) Chen, Q.; Bowman, J. M. Quantum and Classical IR Spectra of $(HCOOH)_2$, $(DCOOH)_2$ and $(DCOOD)_2$ Using *Ab Initio* Potential Energy and Dipole Moment Surfaces. *Faraday Discuss.* **2018**, 33−49.
(5) Garofalini, S. H. Molecular Dynamics Computer Simulations of Silica Surface Structure and Adsorption of Water Molecules. *J. Non-Cryst. Solids* **1990**, *120*, 1−12.
(6) Rai, B.; Sathish, P.; Malhotra, C. P.; Pradip; Ayappa, K. G. Molecular Dynamic Simulations of Self-Assembled Alkylthiolate Monolayers on an Au(111) Surface. *Langmuir* **2004**, *20*, 3138−3144.
(7) Yagi, K.; Taketsugu, T.; Hirao, K. Generation of Full-Dimensional Potential Energy Surface of Intramolecular Hydrogen Atom Transfer in Malonaldehyde and Tunneling Dynamics. *J. Chem. Phys.* **2001**, *115*, 10647−10655.
(8) Doi, M. Molecular dynamics and rheological properties of concentrated solutions of rodlike polymers in isotropic and liquid crystalline phases. *J. Polym. Sci., Polym. Phys. Ed.* **1981**, *19*, 229−243.
(9) Grest, G. S.; Kremer, K. Molecular dynamics simulation for polymers in the presence of a heat bath. *Phys. Rev. A* **1986**, *33*, 3628−3631.
(10) Han, Y.; Elliott, J. Molecular Dynamics Simulations of the Elastic Properties of Polymer/Carbon Nanotube Composites. *Comput. Mater. Sci.* **2007**, *39*, 315−323.
(11) Kremer, K.; Grest, G. S. Dynamics of Entangled Linear Polymer Melts: A Molecular Dynamics Simulation. *J. Chem. Phys.* **1990**, *92*, 5057−5086.
(12) Cheatham, T. E., III; Kollma, P. A. Observation of the A-DNA to B-DNA Transition During Unrestrained Molecular Dynamics in Aqueous Solution. *J. Mol. Biol.* **1996**, *259*, 434−444.
(13) Cheatham, T. E., III; Miller, J. L.; Fox, T.; Darden, T. A.; Kollman, P. A. Molecular Dynamics Simulations on Solvated Biomolecular Systems: The Particle Mesh Ewald Method Leads to Stable Trajectories of DNA, RNA, and Proteins. *J. Am. Chem. Soc.* **1995**, *117*, 4193−4194.
(14) Ding, F.; Sharma, S.; Chalasani, P.; Demidov, V. V.; Broude, N. E.; Dokholyan, N. V. *Ab Initio* RNA Folding by Discrete Molecular Dynamics: From Structure Prediction to Folding Mechanisms. *RNA* **2008**, *14*, 1164−1173.
(15) Karplus, M.; McCammon, J. A. Molecular Dynamics Simulations of Biomolecules. *Nat. Struct. Biol.* **2002**, *9*, 646.
(16) MacKerell, A. D.; Banavali, N. K. All-Atom Empirical Force Field for Nucleic Acids: II. Application to Molecular Dynamics Simulations of DNA and RNA in Solution. *J. Comput. Chem.* **2000**, *21*, 105−120.
(17) Mackerell, A. D.; Feig, M.; Brooks, C. L. Extending the treatment of Backbone Energetics in Protein Force Fields: Limitations of Gas-Phase Quantum Mechanics in Reproducing Protein Conformational Distributions in Molecular Dynamics Simulations. *J. Comput. Chem.* **2004**, *25*, 1400−1415.
(18) Sugita, Y.; Okamoto, Y. Replica-exchange molecular dynamics method for Protein Folding. *Chem. Phys. Lett.* **1999**, *314*, 141−151.
(19) Tieleman, D. P.; Marrink, S.-J.; Berendsen, H. J. A Computer Perspective of Membranes: Molecular Dynamics Studies Of Lipid Bilayer Systems. *Biochim. Biophys. Acta* **1997**, *1331*, 235−270.
(20) van der Ploeg, P.; Berendsen, H. J. C. Molecular dynamics simulation of a Bilayer Membrane. *J. Chem. Phys.* **1982**, *76*, 3271−3276.
(21) Li, J.; Kuppler, R. J.; Zhou, H. Selective gas adsorption and separation in Metal−Organic Frameworks. *Chem. Soc. Rev.* **2009**, *38*, 1477−1504.
(22) Rosenbach, N.; Jobic, H.; Ghoufi, A.; Salles, F.; Maurin, G.; Bourrelly, S.; Llewellyn, P. L.; Devic, T.; Serre, C.; Férey, G. Quasi-Elastic Neutron Scattering and Molecular Dynamics Study of Methane Diffusion in Metal Organic Frameworks MIL-47(V) and MIL-53(Cr). *Angew. Chem., Int. Ed.* **2008**, *47*, 6611−6615.
(23) Skoulidas, A. I. Molecular Dynamics Simulations of Gas Diffusion in Metal−Organic Frameworks: Argon in CuBTC. *J. Am. Chem. Soc.* **2004**, *126*, 1356−1357.
(24) Skoulidas, A. I.; Sholl, D. S. Self-diffusion and transport diffusion of light gases in Metal-Organic Framework Materials Assessed Using Molecular Dynamics Simulations. *J. Phys. Chem. B* **2005**, *109*, 15760−15768.
(25) Yang, Q.; Zhong, C. Molecular Simulation of Adsorption and Diffusion of Hydrogen in Metal−Organic Frameworks. *J. Phys. Chem. B* **2005**, *109*, 11862−11864.
(26) Münch, W.; Seifert, G.; Kreuer, K. D.; Maier, J. A Quantum Molecular Dynamics Study of Proton Conduction Phenomena in $BaCeO_3$. *Solid State Ionics* **1996**, *86*−*88*, 647−652.
(27) Tersoff, J. Modeling Solid-State Chemistry: Interatomic potentials for Multicomponent Systems. *Phys. Rev. B* **1989**, *39*, 5566−5568.
(28) Tycko, R.; Dabbagh, G.; Fleming, R. M.; Haddon, R. C.; Makhija, A. V.; Zahurak, S. M. Molecular Dynamics and the Phase Transition in Solid C_{60}. *Phys. Rev. Lett.* **1991**, *67*, 1886−1889.
(29) Born, M.; Fock, V. Beweis des Adiabatensatzes. *Z. Phys.* **1928**, *51*, 165−180.
(30) Born, M.; Oppenheimer, R. Zur Quantentheorie der Molekeln. *Ann. Phys.* **1927**, *389*, 457−484.
(31) Lopreore, C. L.; Wyatt, R. E. Quantum Wave Packet Dynamics with Trajectories. *Phys. Rev. Lett.* **1999**, *82*, 5190−5193.
(32) Gindensperger, E.; Meier, C.; Beswick, J. A. Mixing Quantum and Classical Dynamics using Bohmian Trajectories. *J. Chem. Phys.* **2000**, *113*, 9369−9372.
(33) Donoso, A.; Zheng, Y.; Martens, C. C. Simulation of Quantum Processes using Entangled Trajectory Molecular Dynamics. *J. Chem. Phys.* **2003**, *119*, 5010−5020.
(34) Donoso, A.; Martens, C. C. Quantum Tunneling using Entangled Classical Trajectories. *Phys. Rev. Lett.* **2001**, *87*, No. 223202.
(35) Waheed, Q.; Edholm, O. Quantum Corrections to Classical Molecular Dynamics Simulations of Water and Ice. *J. Chem. Theory Comput.* **2011**, *7*, 2903−2909.
(36) Varandas, A. J. C.; Marques, J. M. C. Method for Quasiclassical Trajectory Calculations on Potential Energy Surfaces Defined from Gradients and Hessians, and Model to Constrain the Energy in Vibrational Modes. *J. Chem. Phys.* **1994**, *100*, 1908−1920.
(37) Miller, W. H.; Hase, W. L.; Darling, C. L. A Simple Model for Correcting the Zero Point Energy Problem in Classical Trajectory Simulations of Polyatomic Molecules. *J. Chem. Phys.* **1989**, *91*, 2863−2868.
(38) Bowman, J. M.; Gazdy, B.; Sun, Q. A Method to Constrain Vibrational Energy in Quasiclassical Trajectory Calculations. *J. Chem. Phys.* **1989**, *91*, 2859−2862.
(39) Karplus, M.; Porter, R. N.; Sharma, R. D. Exchange Reactions with Activation Energy. I. Simple Barrier Potential for (H, H_2). *J. Chem. Phys.* **1965**, *43*, 3259−3287.
(40) Zheng, J.; Xu, X.; Meana-Pañeda, R.; Truhlar, D. G. Army Ants Tunneling for Classical Simulations. *Chem. Sci.* **2014**, *5*, 2091−2099.
(41) Zheng, J.; Meana-Pañeda, R.; Truhlar, D. G. Including Tunneling in Non-Born−Oppenheimer Simulations. *J. Phys. Chem. Lett.* **2014**, *5*, 2039−2043.
(42) Helgaker, T.; Uggerud, E.; Jensen, H. J. A. Integration of the Classical Equations of Motion on *Ab Initio* Molecular Potential Energy Surfaces Using Gradients and Hessians: Application to Translational Energy Release upon Fragmentation. *Chem. Phys. Lett.* **1990**, *173*, 145−150.
(43) Uggerud, E.; Helgaker, T. Dynamics of the Reaction CH_2OH^+ –> CHO^+ + H_2. Translational Energy Release from Ab Initio Trajectory Calculations. *J. Am. Chem. Soc.* **1992**, *114*, 4265−4268.
(44) Hu, H.; Elstner, M.; Hermans, J. Comparison of a QM/MM force field and Molecular Mechanics Force Fields in Simulations of Alanine and Glycine "Dipeptides" (Ace-Ala-Nme and Ace-Gly-Nme) in Water in Relation to the Problem of Modeling the Unfolded Peptide Backbone in Solution. *Proteins: Struct., Funct., Bioinf.* **2003**, *50*, 451−463.
(45) Albaugh, A.; Boateng, H. A.; Bradshaw, R. T.; Demerdash, O. N.; Dziedzic, J.; Mao, Y.; Margul, D. T.; Swails, J.; Zeng, Q.; Case, D.

DOI: 10.1021/acs.jpca.9b02298
J. Phys. Chem. A 2019, 123, 4543−4554

A.; et al. Advanced Potential Energy Surfaces for Molecular Simulation. *J. Phys. Chem. B* **2016**, *120*, 9811−9832.
(46) Banks, S. T.; Clary, D. C. Reduced Dimensionality Quantum Dynamics of Cl + CH_4 → HCl + CH_3 on an *Ab Initio* Potential. *Phys. Chem. Chem. Phys.* **2007**, *9*, 933−943.
(47) Collins, M. A. Molecular Potential-Energy Surfaces for Chemical Reaction Dynamics. *Theor. Chem. Acc.* **2002**, *108*, 313−324.
(48) Collins, M. A. In *Molecular Potential Energy Surfaces by Interpolation*, International Conference on Computational Science—ICCS 2003, Berlin, Heidelberg, 2003; Springer: Berlin, Heidelberg, 2003; pp 159−167.
(49) Collins, M. A.; Parsons, D. F. Implications of Rotation−Inversion−Permutation Invariance for Analytic Molecular Potential Energy Surfaces. *J. Chem. Phys.* **1993**, *99*, 6756−6772.
(50) Bowman, J. M.; Czakó, G.; Fu, B. High-Dimensional *Ab Initio* Potential Energy Surfaces for Reaction Dynamics Calculations. *Phys. Chem. Chem. Phys.* **2011**, *13*, 8094−8111.
(51) Braams, B. J.; Bowman, J. M. Permutationally invariant potential energy surfaces in High Dimensionality. *Int. Rev. Phys. Chem.* **2009**, *28*, 577−606.
(52) Brown, A.; Braams, B. J.; Christoffel, K.; Jin, Z.; Bowman, J. M. Classical and Quasiclassical Spectral Analysis of CH_5^+ Using An Ab Initio Potential Energy Surface. *J. Chem. Phys.* **2003**, *119*, 8790−8793.
(53) Qu, C.; Yu, Q.; Bowman, J. M. Permutationally Invariant Potential Energy Surfaces. *Annu. Rev. Phys. Chem.* **2018**, *69*, 151−175.
(54) Jiang, B.; Li, J.; Guo, H. Potential Energy Surfaces from high fidelity fitting of *Ab Initio* Points: The Permutation Invariant Polynomial - Neural Network Approach. *Int. Rev. Phys. Chem.* **2016**, *35*, 479−506.
(55) Lorenz, S.; Groß, A.; Scheffler, M. Representing High-Dimensional Potential-Energy Surfaces for Reactions at Surfaces by Neural Networks. *Chem. Phys. Lett.* **2004**, *395*, 210−215.
(56) Manzhos, S.; Dawes, R.; Carrington, T. Neural network-based approaches for Building High Dimensional and Quantum Dynamics-Friendly Potential Energy Surfaces. *Int. J. Quantum Chem.* **2015**, *115*, 1012−1020.
(57) Cui, J.; Krems, R. V. Gaussian process model for collision dynamics of Complex Molecules. *Phys. Rev. Lett.* **2015**, *115*, No. 073202.
(58) Uteva, E.; Graham, R. S.; Wilkinson, R. D.; Wheatley, R. J. Interpolation of Intermolecular Potentials using Gaussian Processes. *J. Chem. Phys.* **2017**, *147*, No. 161706.
(59) Berweger, C. D.; van Gunsteren, W. F.; Müller-Plathe, F. Molecular Dynamics Simulation with an *Ab Initio* Potential Energy Function and Finite Element Interpolation: The Photoisomerization of Cis-Stilbene in Solution. *J. Chem. Phys.* **1998**, *108*, 8773−8781.
(60) Berweger, C. D.; van Gunsteren, W. F.; Müller-Plathe, F. The photoisomerization of Cis-Stilbene Does Not Follow the Minimum Energy Path. *Angew. Chem., Int. Ed.* **1999**, *38*, 2609−2611.
(61) Berweger, C. D.; van Gunsteren, W. F.; Müller−Plathe, F. Finite Element Interpolation for Combined Classical/Quantum Mechanical Molecular Dynamics Simulations. *J. Comput. Chem.* **1998**, *18*, 1484−1495.
(62) Li, W.; Ma, A. Reaction Mechanism and Reaction Coordinates from the Viewpoint of Energy Flow. *J. Chem. Phys.* **2016**, *144*, No. 114103.
(63) Truhlar, D. G.; Garrett, B. C.; Klippenstein, S. J. Current Status of Transition-State Theory. *J. Phys. Chem.* **1996**, *100*, 12771−12800.
(64) Nance, J.; Bowman, D. N.; Mukherjee, S.; Kelley, C. T.; Jakubikova, E. Insights into the Spin-State Transitions in $[Fe(tpy)_2]^{2+}$: Importance of the Terpyridine Rocking Motion. *Inorg. Chem.* **2015**, *54*, 11259−11268.
(65) Nance, J.; Jakubikova, E.; Kelley, C. T. Reaction Path Following with Sparse Interpolation. *J. Chem. Theory Comput.* **2014**, *10*, 2942−2949.
(66) Nance, J.; Kelley, C. A sparse interpolation algorithm for Dynamical Simulations In Computational Chemistry. *SIAM J. Sci. Comput.* **2015**, *37*, S137−S156.
(67) Smolyak, S. A. Quadrature and interpolation formulas for tensor products of Certain Classes of Functions. *Dokl. Akad. Nauk SSSR* **1963**, 1042−1045.
(68) Barbatti, M.; Ruckenbauer, M.; Plasser, F.; Pittner, J.; Granucci, G.; Persico, M.; Lischka, H. Newton-X: A Surface-Hopping Program for Nonadiabatic Molecular Dynamics. *Wiley Interdiscip. Rev.: Comput. Mol. Sci.* **2014**, *4*, 26−33.
(69) Judd, K. L.; Maliar, L.; Maliar, S.; Valero, R. Smolyak method for Solving Dynamic Economic Models: Lagrange Interpolation, Anisotropic Grid and Adaptive Domain. *J. Econ. Dyn. Control* **2014**, *44*, 92−123.
(70) Deriglazov, A. *Classical Mechanics*; Springer, 2016.
(71) Lanczos, C. *The Variational Principles of Mechanics*; Courier Corporation, 2012.
(72) Verlet, L. Computer "experiments" on Classical Fluids. I. Thermodynamical Properties of Lennard-Jones Molecules. *Phys. Rev.* **1967**, *159*, 98−103.
(73) Störmer, C. Sur les Trajectoires des Corpuscules Électrisés dans l'Espace sous l'Action du Magnétisme Terrestre avec Application aux Aurores Boréales. *Arch. Sci. Phys. Nat.* **1912**, *33*, 51−69.
(74) Feng, K.; Qin, M.-z. In *The Symplectic Methods for the Computation of Hamiltonian Equations*, Numerical Methods for Partial Differential Equations: Proceedings of a Conference Held in Shanghai, P. R. China, March 25−29, 1987; Zhu, Y.-I., Zhu, Y.-I., Guo, B.-y., Eds.; Springer: Berlin, Heidelberg, 1987; pp 1−37.
(75) Sanz-Serna, J. M. Symplectic Integrators for Hamiltonian Problems: An Overview. *Acta Numer.* **1992**, *1*, 243−286.
(76) Hünenberger, P. H. Thermostat Algorithms for Molecular Dynamics Simulations. In *Advanced Computer Simulation: Approaches For Soft Matter Sciences I*; Holm, C., Kremer, K., Eds.; Advances in Polymer Science; Springer: Berlin, Heidelberg, 2005; Vol. *173*, pp 105−149.
(77) Andersen, H. C. Molecular Dynamics Simulations at Constant Pressure and/or Temperature. *J. Chem. Phys.* **1980**, *72*, 2384−2393.
(78) Schneider, T.; Stoll, E. Molecular-Dynamics Study of a Three-Dimensional One-Component Model for Distortive Phase Transitions. *Phys. Rev. B* **1978**, *17*, 1302−1322.
(79) Allen, M. P.; Tildesley, D. J. *Computer Simulation of Liquids*; Oxford University Press, 2017.
(80) Leimkuhler, B.; Matthews, C. Robust and Efficient Configurational Molecular Sampling via Langevin Dynamics. *J. Chem. Phys.* **2013**, *138*, No. 174102.
(81) Leimkuhler, B.; Matthews, C. Rational Construction of Stochastic Numerical Methods for Molecular Sampling. *Appl. Math. Res. eXpress* **2013**, *2013*, 34−56.
(82) Frisch, M. J.; Trucks, G. W.; Schlegel, H. B.; Scuseria, G. E.; Robb, M. A.; Cheeseman, J. R.; Scalmani, G.; Barone, V.; Mennucci, B.; Petersson, G. A. et al. *Gaussian 09*; Gaussian, Inc.: Wallingford, CT, 2009.
(83) Becke, A. D. A New Mixing of Hartree−Fock and Local Density-Functional Theories. *J. Chem. Phys.* **1993**, *98*, 1372−1377.
(84) Becke, A. D. Density-Functional Thermochemistry. III. The Role of Exact Exchange. *J. Chem. Phys.* **1993**, *98*, 5648−5652.
(85) Lee, C.; Yang, W.; Parr, R. G. Development of the Colle-Salvetti Correlation-Energy Formula into a Functional of the Electron Density. *Phys. Rev. B* **1988**, *37*, 785−789.
(86) Stephens, P. J.; Devlin, F. J.; Chabalowski, C. F.; Frisch, M. J. *Ab Initio* Calculation of Vibrational Absorption and Circular Dichroism Spectra Using Density Functional Force Fields. *J. Phys. Chem.* **1994**, *98*, 11623−11627.
(87) Francl, M. M.; Pietro, W. J.; Hehre, W. J.; Binkley, J. S.; Gordon, M. S.; DeFrees, D. J.; Pople, J. A. Self-Consistent Molecular Orbital Methods. XXIII. A Polarization-Type Basis Set for Second-Row Elements. *J. Chem. Phys.* **1982**, *77*, 3654−3665.
(88) Hariharan, P. C.; Pople, J. A. The Influence of Polarization Functions on Molecular Orbital Hydrogenation Energies. *Theoret. Chim. Acta* **1973**, *28*, 213−222.
(89) Hehre, W. J.; Ditchfield, R.; Pople, J. A. Self-Consistent Molecular Orbital Methods. XII. Further Extensions of Gaussian-

DOI: 10.1021/acs.jpca.9b02298
J. Phys. Chem. A 2019, 123, 4543−4554

Type Basis Sets for use in Molecular Orbital Studies of Organic Molecules. *J. Chem. Phys.* **1972**, *56*, 2257−2261.
(90) McQuarrie, D. A. *Statistical Thermodynamics*; Harper and Row: New York, 1973.
(91) Craver, C. D. *The Coblentz Society Desk Book of Infrared Spectra*; National Standard Reference Data System, 1977.
(92) Münster, A. *Statistical Thermodynamics*; Springer, 1969.
(93) Hill, C.; Yurchenko, S. N.; Tennyson, J. Temperature-Dependent Molecular Absorption Cross Sections for Exoplanets and Other Atmospheres. *Icarus* **2013**, *226*, 1673−1677.
(94) Tennyson, J.; Yurchenko, S. N. ExoMol: Molecular Line Lists for exoplanet and Other Atmospheres. *Mon. Not. R. Astron. Soc.* **2012**, *425*, 21−33.
(95) Yurchenko, S. N.; Barber, R. J.; Tennyson, J. A Variationally Computed Line List for Hot NH_3. *Mon. Not. R. Astron. Soc.* **2011**, *413*, 1828−1834.
(96) Good, W. E. The Inversion Spectrum of Ammonia. *Phys. Rev.* **1946**, *70*, 213−218.
(97) Hoff, D. A.; da Silva, R.; Rego, L. G. C. Coupled Electron−Hole Quantum Dynamics on D−π−A Dye-Sensitized TiO_2 Semiconductors. *J. Phys. Chem. C* **2012**, *116*, 21169−21178.
(98) Monti, A.; Negre, C. F. A.; Batista, V. S.; Rego, L. G. C.; de Groot, H. J. M.; Buda, F. Crucial Role of Nuclear Dynamics for Electron Injection in a Dye−Semiconductor Complex. *J. Phys. Chem. Lett.* **2015**, *6*, 2393−2398.
(99) Towns, J.; Cockerill, T.; Dahan, M.; Foster, I.; Gaither, K.; Grimshaw, A.; Hazlewood, V.; Lathrop, S.; Lifka, D.; Peterson, G. D.; et al. XSEDE: Accelerating Scientific Discovery. *Comput. Sci. Eng.* **2014**, *16*, 62−74.

DOI: 10.1021/acs.jpca.9b02298
J. Phys. Chem. A 2019, 123, 4543−4554